applied sciences

Article

Modeling and Optimization of Wireless Signal Transmission Characteristics of Mine Roadway Based on 3D Ray-Tracing Method

Boyu Li [1], Tao Ding [2,]*, Yanhui Wu [3], Zhen Nie [2], Qian Wu [2], Yannan Shi [1,4,]* and Mianping Zheng [2]

[1] School of Mechanical and Equipment Engineering, Hebei University of Engineering, Handan 056038, China; roald6677@163.com
[2] Key Laboratory of Saline Lake Resources and Environment (Ministry of Natural Resources), Institute of Mineral Resources, Chinese Academy of Geological Sciences, Beijing 100037, China; nieezhen518@163.com (Z.N.); wuqian0516@163.com (Q.W.); zhengmp2010@126.com (M.Z.)
[3] School of Mining and Geomatics Engineering, Hebei University of Engineering, Handan 056038, China; wuyh_198210@163.com
[4] Collaborative Innovation Center for Modern Equipment Manufacturing of Jinan New Area (Hebei), Handan 056038, China
* Correspondence: dtcumtb@163.com (T.D.); shiynchn@163.com (Y.S.); Tel.: +86-10-6899-2231 (T.D.)

Abstract: The mine roadway is a special restricted space where wireless signals cannot freely propagate. The research on the transmission characteristics of wireless signals in mine roadways is of great significance for establishing a safe and reliable underground communication system. In this context, the transmission characteristics of wireless signals with a frequency of 700 MHz in the roadway are studied using the three-dimensional (3D) ray-tracing method. The calculation of the vertical dimension of the roadway is increased, and a roadway model is established to more comprehensively reflect the transmission characteristics of the signal in the roadway. The results show that the field strength in the near-source region is high, the attenuation is fast, and the fluctuation is strong, while the waveform in the far-source region gradually stabilizes and decays. The signal strength is related to the number of reflections; the more reflections, the weaker the signal strength. When the transmitting end is close to the edge of the roadway wall, the signal attenuation is faster and the fluctuation amplitude is stronger. The signal strength in the roadway is affected by the cross-sectional size of the rectangular roadway, and the larger the length and width dimensions, the better the waveguide can be formed in the roadway. The simulation results of wireless signal transmission in the roadway are compared with the measured results from a coal mine in Ganhe, Huozhou, and the results show that the model established by the 3D ray-tracing method can predict the field strength distribution of wireless signal. This study provides a theoretical foundation and practical guidance for improving the reliability and quality of wireless signal transmission in mine tunnels. Future research directions can further optimize algorithms, enhance transmission rates, and improve interference resistance to meet the needs of wireless communication in mine tunnels.

Keywords: 3D ray-tracing; mine roadways; ray-tracing models; wireless signal; transmission characteristic modeling

Citation: Li, B.; Ding, T.; Wu, Y.; Nie, Z.; Wu, Q.; Shi, Y.; Zheng, M. Modeling and Optimization of Wireless Signal Transmission Characteristics of Mine Roadway Based on 3D Ray-Tracing Method. *Appl. Sci.* **2024**, *14*, 1534. https://doi.org/10.3390/app14041534

Received: 16 January 2024
Revised: 4 February 2024
Accepted: 7 February 2024
Published: 14 February 2024

1. Introduction

Coal is the primary source of energy worldwide and plays a crucial role in industrial production [1,2]. To ensure safe production, efficient management, and emergency response in coal mines, it is of great significance to establish a reliable and efficient underground communication system [3–5]. The establishment of a safe and reliable wireless communication system in the limited space of coal mine tunnels is a hot research topic in coal production.

At present, most mine communication and coordination systems use wired production dispatch communication systems, pager systems, low-frequency leak communication systems (60 MHz, 80 MHz, and 150 MHz), amplification broadcast systems used at the working face, as well as communication products based on Wi-Fi, WiMAX, and SCDMA technologies [6–10]. However, the wired communication is installed at fixed locations, while most workers perform dynamic operations. In the event of a mine disaster requiring communication and coordination, leaks often occur, and pager systems have the disadvantage of unstable signals, making it difficult for them to serve as an emergency communication tool. This prevents employees in danger from receiving evacuation information in a timely manner and evacuating promptly. As for the low-frequency leakage communication at 60 MHz, 80 MHz, and 150 MHz, due to the special underground environment, the use of a large number of frequency converters, the operation of overhead line locomotives, and the operation of high-power motors generate electromagnetic interference, resulting in poor call quality, loud noise, excessive interference, and high failure rates. They are not suitable for daily production scheduling communication and coordination in mines [11,12]. Communication products based on Wi-Fi, wimax, and SCDMA technologies are civilian products introduced for underground use and are not industrial-specific communication systems [13–15]. Due to the special environment of mines, further research is needed to study the wireless signal transmission characteristics in coal mine tunnels and establish a comprehensive and accurate wireless signal propagation model to ensure the stable operation of underground mine communication systems.

The ray-tracing method and its hybrid versions are often used when studying the wireless signal transmission characteristics of mine roadways. The ray-tracing methods mainly include the image method and the shooting and bouncing ray (SBR) method. Ref. [16] improved the ray-tracing method and studied the transmission characteristics of wireless signals at two frequencies, 2.45 GHz and 5.7 GHz, in subway tunnels. In the improved ray-tracing method, the surface of the intersection point of the ray path, and the environment can be determined in advance, which improves the algorithm's efficiency. The calculation accuracy of the image method is related to the number of images, i.e., more images lead to a greater number of reflection points and reflection lines. As a result, the computational complexity of the image method increases dramatically with an increase in the number of images [17]. Ref. [18] used the image method to establish a multipath model for a rectangular wireless signal in a coal mine, conducted simulations on the field strength at the receiving point, and simulated the transmission of ultrahigh-frequency (UHF) signals in the roadway. However, in complex roadway environments, the computational efficiency of imaging methods is poor. In the SBR method, the signal-receiving end is imagined as a very small circular area, the ray paths that reach the circular area are considered effective paths, and discrete ray trajectories are obtained based on the model. By introducing the height of the vector antenna, Ref. [19] used the SBR method to calculate the additional loss caused by the shape of the tunnel, such as a curve. Refs. [20,21] utilize a hybrid algorithm composed of a recursive neural network (LSTM), an annealing algorithm, and a support vector machine (SVM) to establish a model for tunnel wireless signal loss and conduct field strength prediction. The results demonstrate the feasibility of SVM application in tunnels and its superiority in accuracy over traditional signal fading models. When support vector machines are used for model prediction, the prediction time is related to the number of support vectors. When the number of support vectors is large, the computational complexity is great. The hybrid ray-tracing model addresses the issue of a single model not simulating signal transmission characteristics well. Ref. [22] combined the ray-tracing model and the waveguide model, i.e., using the waveguide modeling method in the near-source region and the ray-tracing modeling method in the far-source region. This method improves the accuracy of the channel model but increases its complexity, and signal transmission in roadways is a continuously changing process; as a result, there is no obvious boundary condition for determining the near-source region or far-source region.

To solve these problems, this paper proposes to use three-dimensional (3D) ray-tracing methods for studying the transmission characteristics of wireless signals in coal mine roadways. This study analyzes the effects of complex roadway environments (such as rough roadway walls) and lossy media (such as dust and fog droplets) on wireless signal attenuation and assesses the effects of parameters, such as transceiver antenna position and antenna gain, signal incidence angle, and the number of reflections, on the wireless signal field strength. This research will provide a theoretical foundation and practical guidance for the design and optimization of mine roadway communication systems. At the same time, it will also play a significant role in promoting research into the application of wireless signals in similar complex environments.

2. Three-Dimensional Ray-Tracing Model

2.1. Three-Dimensional Ray-Tracing and Acceleration Algorithm

The ray-tracing method is widely used to study the propagation characteristics of wireless signals in a confined space [23,24]. The ray-tracing method for tracking the path of wireless signals in roadways can be divided into three parts: wireless signal transmission, solving for the intersection point of the signal path with the reflection plane, and receiver receiving. During the transmission process, the wireless signal can undergo reflection and refraction, which can cause energy loss. A signal that has undergone more than three reflections can suffer severe energy loss. When calculating the field strength at the receiving point, it is suitable to select effective paths with three or fewer reflections for the calculations [17]. A flow chart of the 3D ray-tracing method is shown in Figure 1. Y is the input signal. The signal is decomposed into n signaling components, and the transmission paths of the n signaling components are traced. Then, the field strengths of signaling components that can reach the receiving end are superimposed to obtain the wireless signal strength P at the receiving end.

The calculation of the vertical dimension is added to the 3D ray-tracing method, the established roadway model is more complete, and the obtained wireless signal transmission characteristics are more comprehensive. However, this method incurs an exponentially increasing amount of computation for simulation and actual application. Therefore, the spatial segmentation algorithm is added to the 3D ray-tracing algorithm to overcome the large computational complexity of the 3D ray-tracing algorithm.

In the spatial segmentation-based acceleration algorithm, the roadway model is divided into several cubes, and each transmission path of the wireless signal is distributed in some of the divided cubes. When a transmission path of wireless signals reaches a certain cube, intersection detection must be performed only on the adjacent cubes. If the ray intersects the adjacent cube, the cube is regarded as valid, the occurrence of reflection or refraction is determined, and then the algorithm continues to track the next adjacent cube. If the ray does not intersect one adjacent cube, the other adjacent cube is checked again. As shown in Figure 2, the path of the wireless signal from point M to point N contains only cubes 1, 2, and 3. Therefore, it is only necessary to trace and calculate the effects of planes 11, 12, 21, 22, 31, and 32 on the strength and path of the ray. After the roadway space is divided, the tracing of the ray path does not have to cover all the roadway planes, which greatly improves the computational efficiency of the 3D ray-tracing method.

2.2. Total Transmission Loss

Due to the complex underground environment of coal mines, the wireless signal transmission process is subjected to rough loss and tilt loss caused by reflection, refraction, and scattering from the rough wall of the roadway and dielectric loss caused by reflection of lossy media such as dust and mist in the roadway. The shape and size of the roadway cause the signal pattern to attenuate; thus, the equation for total attenuation of the wireless signal in the roadway is:

$$A_{total} = A_r + A_t + A_a + A_{E_{mn}^{(h)}} \tag{1}$$

where A_{total} is the total loss of the wireless signal, A_r is the roughness loss, A_t is the tilt loss, A_a is the dielectric loss, and $A_{E_{mn}^{(hv)}}$ is the mode attenuation loss.

Based on waveguide theory, the attenuation equations for horizontally and vertically polarized waves are:

$$\begin{aligned} A_{E_{\mathrm{mn}}^{(\mathrm{k})}} &= 4.343\lambda^2 z\left(\frac{m^2\varepsilon_1}{a^3\sqrt{\varepsilon_1-1}} + \frac{n^2}{b^3\sqrt{\varepsilon_2-1}}\right) \\ A_{E_{\mathrm{mn}}^{(v)}} &= 4.343\lambda^2 z\left(\frac{m^2}{a^3\sqrt{\varepsilon_1-1}} + \frac{n^2\varepsilon_2}{b^3\sqrt{\varepsilon_2-1}}\right) \end{aligned} \quad (2)$$

where m is the half wavenumber in the horizontal direction, n is the half wavenumber in the vertical direction, z is the distance from the transmitting end, and a and b are the width and height of the rectangular roadway, respectively. Assuming that the material of the roadway wall is the same and the distribution is even, i.e., $\varepsilon_1 = \varepsilon_2 = \varepsilon$, and $\tau = a/b$ represents the ratio of the width to the height of the roadway. Equation (2) can be rewritten as

$$\begin{aligned} A_{E_{\mathrm{mn}}^{(\mathrm{k})}} &= 4.343\lambda^2 z\frac{m^2\varepsilon+n^2\tau^3}{a^3\sqrt{\varepsilon-1}} \\ A_{E_{\mathrm{mn}}^{(v)}} &= 4.343\lambda^2 z\frac{m^2+n^2\varepsilon\tau^3}{a^3\sqrt{\varepsilon-1}} \end{aligned} \quad (3)$$

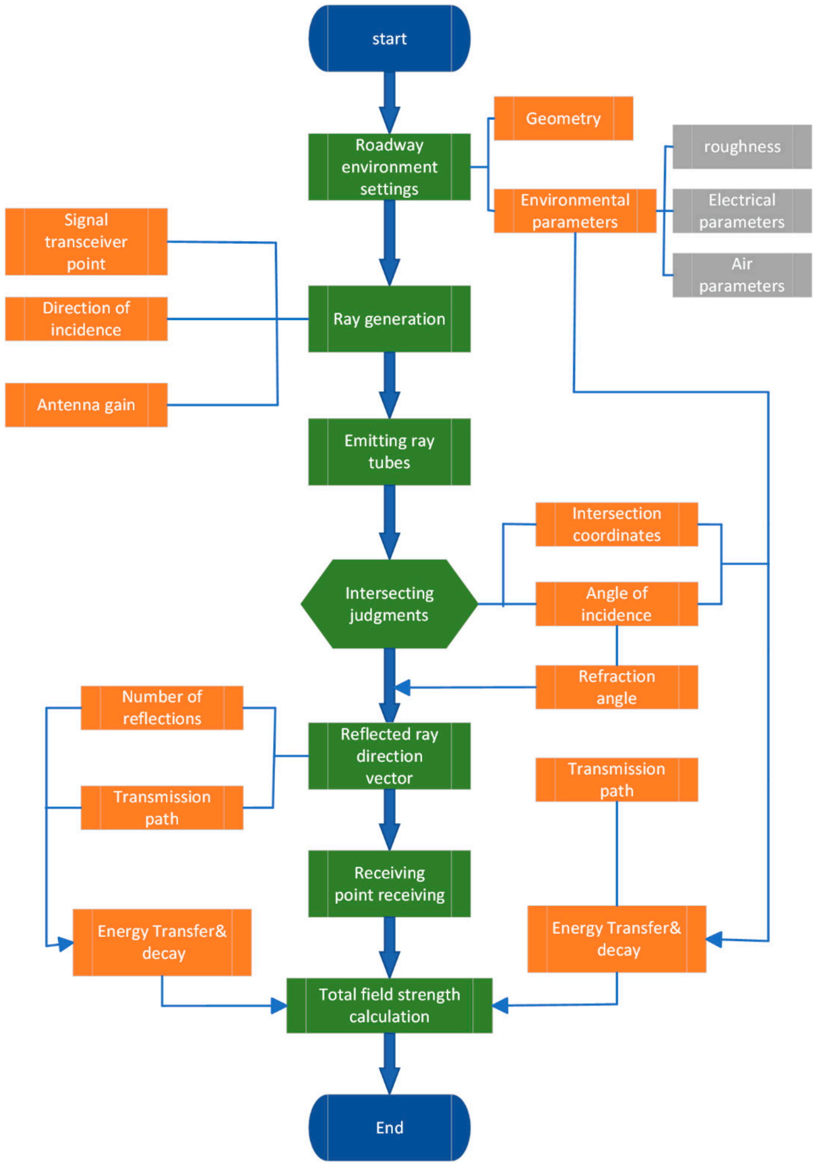

Figure 1. Three-dimensional ray tracing flowchart.

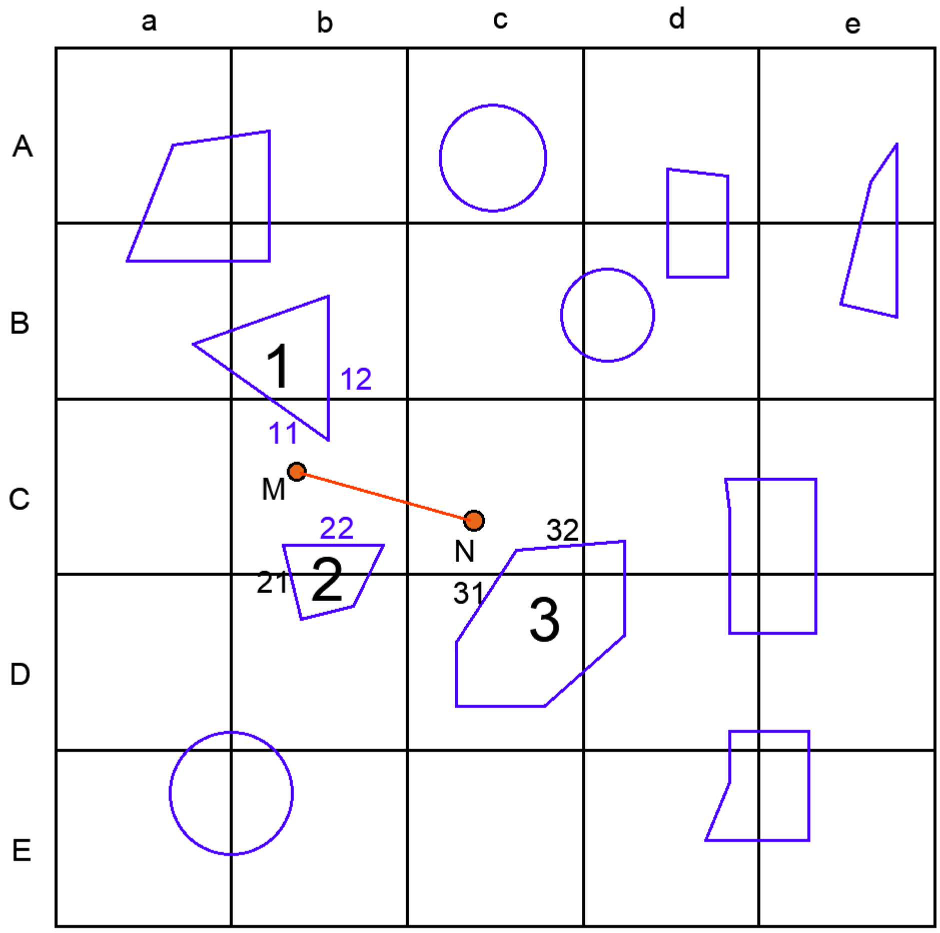

Figure 2. Schematic diagram of spatial segmentation. (The different blue forms represent objects that are divided by spatial segmentation. The orange line is the transmission path of the signal. The orange dots M and N are the start and end points of the signal transmission path. 1, 2, 3, 11, 12, 21, 22, 31, 32 are the different objects and surfaces involved in the transmission path).

Rough roadway walls can cause reflection, refraction, and scattering, which causes the outward diffusion of wireless signal energy and energy loss. The effect of roadway wall roughness on a wireless signal is given in Ref. [25]:

$$A_R = 8.636\pi^2 \Delta h^2 z\left(\frac{1}{a^4} + \frac{1}{b^4}\right) \tag{4}$$

where Δh is the average roughness/height of the roadway.

The tilt of the roadway wall converts a part of the energy of the main mode of the wireless signal, and the transmission of the main mode generates loss. Assuming that the tilt angle of the roof and sidewall of the coal mine roadway is θ, the expression of the tilt loss is rewritten as:

$$A_{\mathrm{t}} = \frac{4.343\pi^2\theta^2 \mathrm{z}}{2\lambda}(\mathrm{m}+\mathrm{n}) \tag{5}$$

In addition to the size factors of the roadway, the mode attenuation of the wireless signal is related to the medium used for the roadway. The electromagnetic characteristics of the medium used for the roadway mainly include the permittivity ε, magnetic permeability μ and conductivity σ. When studying the effect of the medium on wireless signal attenuation, the complex relative permittivity can be expressed as:

$$\varepsilon_r{}' = \varepsilon_r + \frac{\sigma}{jw\varepsilon_0} \tag{6}$$

where ε_r is the permittivity, $\varepsilon_{r'}$ is the complex relative permittivity, and ε_0 is the vacuum permittivity. The expression for propagation attenuation can be derived as follows:

$$\begin{aligned} PA_{E_{mn}^{(\mathrm{h})}} &= 4.343\lambda^2 z\mathrm{Re}\left(\frac{m^2\varepsilon'_{r1}}{a^3\sqrt{\varepsilon'_{r1}-1}} + \frac{\mathrm{n}^2}{b^3\sqrt{\varepsilon'_{r2}-1}}\right) - 4.343\frac{\lambda^2}{2\pi}z\mathrm{Im}\left(\frac{m^2{\varepsilon'_{r1}}^2}{a^4\sqrt{\varepsilon'_{r1}-1}} - \frac{\mathrm{n}^2}{b^4\sqrt{\varepsilon'_{r2}-1}}\right) \\ PA_{E_{mn}^{(\mathrm{r})}} &= 4.343\lambda^2 z\mathrm{Re}\left(\frac{m^2\varepsilon'_{r1}}{a^3\sqrt{\varepsilon'_{r1}-1}} + \frac{\mathrm{n}^2\varepsilon'_{r2}}{b^3\sqrt{\varepsilon'_{r2}-1}}\right) - 4.343\frac{\lambda^2}{2\pi}z\mathrm{Im}\left(\frac{m^2}{a^4\sqrt{\varepsilon'_{r1}-1}} - \frac{\mathrm{n}^2{\varepsilon'_{r1}}^2}{b^4\sqrt{\varepsilon'_{r2}-1}}\right) \end{aligned} \tag{7}$$

The formula for total signal loss during transmission in a tunnel is:

$$\begin{aligned} A_{\mathrm{total}} &= 4.343\lambda^2 z\left(\frac{m^2\varepsilon_1}{a^3\sqrt{\varepsilon_1-1}} + \frac{n^2}{b^3\sqrt{\varepsilon_2-1}}\right) + 8.636\pi^2\Delta h^2 z\left(\frac{1}{a^4} + \frac{1}{b^4}\right) \\ &+ \frac{4.343\pi^2\theta^2 z}{2\lambda}(\mathrm{m}+\mathrm{n}) + 4.343\lambda^2 z\mathrm{Re}\left(\frac{m^2\varepsilon'_{r1}}{a^3\sqrt{\varepsilon'_{r1}-1}} + \frac{\mathrm{n}^2}{b^3\sqrt{\varepsilon'_{r2}-1}}\right) \end{aligned} \tag{8}$$

2.3. Path Correction of the Multipath Transmission Model

The ray optics method is applicable in optical waveguides when the geometric dimensions of the object are much larger than the wavelength. This principle is similar to the propagation of wireless signals in mines. Therefore, using the ray optics analysis method to analyze the propagation of wireless signals in tunnels is an effective approach.

Based on the fundamental laws of similarity between super-high-frequency electromagnetic waves and light, as well as light transmission, it is possible to derive the attenuation formula for electromagnetic wave transmission in the optical model [26].

$$A(\mathrm{dB}) = 10\lg P_i/P_r = 10\lg\left[(\lambda/4\pi)^2\left|\frac{G_d}{L_d} + \sum\frac{G_i R_i \exp\left(j\frac{2\pi}{\lambda}(L_i - L_d)\right)}{L_r}\right|^2\right] \tag{9}$$

where A is the attenuation of electromagnetic waves. G_d represents the total gain of the transmitting antenna for the Line-of-Sight (LOS) path, and G_i represents the total gain of the receiving antenna for the i-th path. R_i represents the product of reflection coefficients experienced by the i-th path. L_d represents the propagation distance for the direct path, and L_i represents the propagation distance for the i-th path. According to the formula, it can be concluded that the field strength distribution in the tunnel is related to the number of effective rays reaching the receiving point, the lengths of different ray paths, the number of reflections, and the reflection coefficients.

According to the ray theory, if the wavelength of the wireless signal is significantly smaller than the cross-sectional size of the mine tunnel, the geometric optical ray method can be employed to determine each path between the transmitter and receiver in the multipath channel.

The four reflective effects of the walls in the alley are equivalent to two planar waveguides: One planar waveguide is formed by the left and right walls, creating a vertical waveguide, and the other is created by the upper and lower walls, forming a horizontal waveguide. Without considering reflections and scattering from other obstacles within the alley, the total number of signal paths at the receiving point (n) includes one refracted path and $4m$ ray paths reflected by the four alley walls, represented as $n = 4m + 1$. By employing Equation (9) and considering the length of each reflection path, it is possible to determine the transmission loss for each ray. From this, the total power at the receiving point and the total transmission loss can be obtained.

The total power at the receiving point is given by:

$$\begin{cases} P = P_T\left|\frac{\lambda}{4\pi L_d}\right|^2 G_T G_R\left|1 + \sum_{i=1}^{m}\sum_{l=1}^{n}\prod_{k=1}^{i} R_{ilk}^{(\pm)}\exp(j\Delta\varphi_{il})\right|^2 \\ \Delta\varphi_{il} = 2\pi\Delta L/\lambda \end{cases} \tag{10}$$

In the formula, P represents the total received power at the receiving point, P_T represents the transmit antenna power, L_d is the direct path length in kilometers, f is the wireless signal frequency in MHz, and G_T and G_R are the gains of the transmitting and receiving antennas, respectively. n and m represent the odd and even numbers of reflection times respectively, $R_{ilk}^{(\pm)}$ represents the reflection coefficient for each reflection, $\Delta\varphi_{il}$ represents the phase difference between the l-th reflection path in the i-th reflection and the direct path L_d, $\Delta\varphi_{il} = 2\pi\Delta L/\lambda$.

The total transmission loss is calculated as follows:

$$\begin{gathered}[A_g](\mathrm{dB}) = 10\lg\frac{P_T}{P_R} = 32.44 + 20\lg L_d + 20\lg f - 10\lg(G_T G_R) - \\ 20\lg\left|1 + \sum_{i=1}^{m}\sum_{l=1}^{n}\prod_{k=1}^{i} R_{ilk}^{(\pm)}\exp(j\Delta\varphi_{il})\right|\end{gathered} \tag{11}$$

where P_R is the received power.

According to Equation (11), it can be seen that the total transmission loss in the mine tunnel is composed of two parts: one part is the LOS (Line-of-Sight)-free space propagation loss, which is related to the signal operating frequency, transmission distance L_d, antenna transmission gain G_T, and G_R; the other part is the path loss.

However, the multipath channel model established based on the plane waveguide method only considers the losses during signal transmission along the plane and cannot accurately reflect the actual field strength at the receiving point. Therefore, it is necessary to analyze the transmission loss of the zigzag helical ray. By applying Fermat's principle and the first and second tent laws, the total path of the zigzag helical ray can be calculated.

In the case of wireless signals from the base station and the receiving end, they are sent directly to the receiving end. However, wireless signals on the top and bottom plates of the tunnel, as well as on both sides, undergo multiple reflections before reaching the receiving end. Considering the scenarios where wireless signals undergo multiple reflections and scattering, the final result can be obtained.

$$\begin{gathered}[A_g](\mathrm{dB}) = 32.44 + 20\lg L_d + 20\lg f - 10\lg(G_T G_R) \\ -20\lg\left|1 + \sum_{i=1}^{m}\sum_{l=1}^{n}\prod_{k=1}^{i} R_{ilk}^{(\pm)}\exp(j\Delta\varphi_{il}) + \sum_{n=1}^{N}\prod_{k=1}^{K} R_{nk}^{(\pm)}\exp(j\Delta\varphi_{n})\right|\end{gathered} \tag{12}$$

The path loss model is further modified according to Equations (8) and (12), and the following results are obtained:

$$\begin{gathered}[A_g](\mathrm{dB}) = 32.44 + 20\lg L_\mathrm{d} + 20\lg f + L_{total} - 10\lg(G_T G_R) - \\ 20\lg\left|1 + \sum_{i=1}^{m}\sum_{l=1}^{n}\prod_{k=1}^{i} R_{ilk}^{(\pm)}\exp(j\Delta\varphi_{il}) + \sum_{n=1}^{N}\prod_{k=1}^{K} R_{nk}^{(\pm)}\exp(j\Delta\varphi_{n})\right|\end{gathered} \tag{13}$$

During wireless signal propagation, various factors contribute to signal attenuation. To enhance the accuracy of measuring propagation distance, additional adjustments can be made to Equation (13) by incorporating the correction factor ΔL. The formula after correction is as follows:

$$\begin{gathered}[A_g](\mathrm{dB}) = 32.44 + 20\lg L_\mathrm{d} + 20\lg f + L_{total} + \Delta L - 10\lg(G_T G_R) - \\ 20\lg\left|1 + \sum_{i=1}^{m}\sum_{l=1}^{n}\prod_{k=1}^{i} R_{ilk}^{(\pm)}\exp(j\Delta\varphi_{il}) + \sum_{n=1}^{N}\prod_{k=1}^{K} R_{nk}^{(\pm)}\exp(j\Delta\varphi_{n})\right|\end{gathered} \tag{14}$$

Through derivation, the L_d expression of wireless signal propagation distance in the well can be obtained:

$$\begin{cases} L_\mathrm{d} = 10^{\mathrm{a}+b-c-d} \\ a = -1.622 - \lg f - [A_g]/2 + \lg(G_T G_R)/2 \\ b = \lg\left|1 + \sum\limits_{i=1}^{m}\sum\limits_{l=1}^{n}\prod\limits_{k=1}^{i} R_{ilk}^{(\pm)}\exp(j\Delta\varphi_{il}) + \sum\limits_{n=1}^{N}\prod\limits_{k=1}^{K} R_{nk}^{(\pm)}\exp(j\Delta\varphi_{n})\right| \\ c = L_{total} \\ d = \Delta L \end{cases} \tag{15}$$

From the formula, it can be seen that the propagation distance L_d of the signal underground is composed of four parts: the first part is the free propagation loss, which is related to the operating frequency, antenna transmission gain, etc.; the second part is the transmission loss of the synthesized signal from multiple paths; the third part is related to the specific environment underground, such as tunnel cross-section, roughness, etc.; and the fourth part is related to the correction factor ΔL.

The correction factor ΔL exhibits different values in different underground environments and can be obtained by using the principle of a support vector machine with least squares support. The support vector machine algorithm constructs the optimal classification plane based on linear separability and limited sample information, separating samples of different classifications while considering model complexity and accuracy [20,21,27,28].

As shown in Figure 3, the sample data to be segmented are divided into two parts, L1 and L2, with the distance between them called the classification margin. The optimal classification line can be obtained when the classification margin is maximized. When extended to high-dimensional space, it becomes the optimal classification hyperplane.

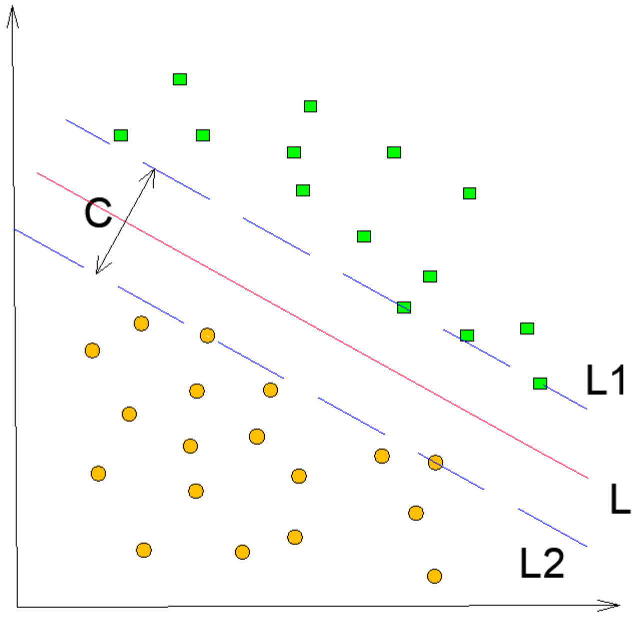

Figure 3. SVM hyperplane partition. (Orange dots and green squares are different samples. L, L1 and L2 are classification lines. C is classification margin).

For a linearly separable problem, let the training samples be represented as $D = \left\{(\vec{x_1}, y_1), (\vec{x_2}, y_2) \cdots (\vec{x_i}, y_i), i = 1, 2, 3 \cdots m\right\}$, y∈{+1,−1}. Here, $\vec{x_i}$ represents the i-th sample feature variable, and y_i is the corresponding desired output.

Correspondingly, the support vector classification interval C=$2/\left\|\vec{\omega}\right\|$ is required to accommodate two different categories, $\vec{\omega}$ is hyperplanar normal, and the objective hyperplane requires minimizing $\left\|\vec{\omega}\right\|^2/2$ by maximizing the support vector interval. This leads to a quadratic programming problem, namely:

$$\begin{cases} \min \frac{1}{2}\left\|\vec{\omega}\right\|^2 \\ s.t. y_i(\vec{\omega}^T \vec{x_i} + b) \geq 1, i = 1, 2, 3 \cdots m \end{cases} \tag{16}$$

where b is the intercept of the hyperplane. By introducing the Lagrange function transformation, we can obtain:

$$L(\vec{\omega}, b, \vec{\alpha}) = \frac{1}{2}\left\|\vec{\omega}\right\|^2 - \sum_{i=1}^{m} \alpha_i \left[y_i(\vec{\omega}^T \vec{x_i} + b) - 1\right] \tag{17}$$

In Equation (19), $\vec{\alpha} = (\alpha_1, \alpha_2, \cdots \alpha_m)^T$ represents the Lagrange multiplier, and $L(\vec{\omega}, b, \vec{\alpha})$ is a convex quadratic function associated with $\vec{\omega}$. We differentiate with respect to $\vec{\omega}$ and b, and substitute them into the Lagrangian expression, then simplify it.

$$L(\vec{\omega}, b, \vec{\alpha}) = \sum_{i=1}^{m} \alpha_i - \frac{1}{2}\sum_{i=1}^{m}\sum_{j=1}^{m} y_i y_j \alpha_i \alpha_j \vec{x_i}^T \vec{x_j} \tag{18}$$

The corresponding duality problem is obtained through the change of Lagrange function:

$$\begin{cases} \max L(\vec{\omega}, b, \vec{\alpha}) = \sum\limits_{i=1}^{m} \alpha_i - \frac{1}{2}\sum\limits_{i=1}^{m}\sum\limits_{j=1}^{m} y_i y_j \alpha_i \alpha_j \vec{x_i}^T \vec{x_j} \\ s.t. \sum\limits_{i=1}^{m} \alpha_i y_i = 0, \alpha \geq 0, i = 1, 2, 3, \cdots, m \end{cases} \tag{19}$$

Utilizing quadratic programming to solve this problem, assuming $\vec{\alpha_i^*} = (\alpha_1^*, \alpha_2^*, \cdots \alpha_m^*)^T$ as the global optimal solution, we can obtain:

$$\begin{cases} \vec{\omega}^* = \sum\limits_{i=1}^{m} \vec{\alpha_i^*} y_i \vec{x_i} \\ b^* = y_i - \sum\limits_{i=1}^{m} \vec{\alpha_i^*} y_i (\vec{x_i}, \vec{x_j}) \\ b^* = -(\vec{\omega}^* \sum\limits_{i=1}^{m} \vec{\alpha_i^*} \vec{x_i}) / (2 \sum\limits_{i=1} \vec{\alpha_i^*}) \end{cases} \tag{20}$$

Finally, the decision function is obtained:

$$f(x) = \mathrm{sgn}(\vec{\omega}^{*T} \vec{x} + b^*) = \mathrm{sgn}\left[\sum_{i=1}^{m} \alpha_i y_i (\vec{x_i}, \vec{x}) + b\right] \tag{21}$$

For the problem of linearly inseparable support vector machines, the introduction of slack variables ζ ($\zeta_i \geq 0, i = 1, 2, \cdots m$) and penalty factor C ($C > 0$) transforms the objective function and constraints into the dual problem as follows:

$$\begin{cases} \max L(\vec{\omega}, b, \vec{a}) = \sum\limits_{i=1}^{m} a_1 - \frac{1}{2}\sum\limits_{i=1 j=1}^{m} y_i y_j a_i a_j K\left(\vec{x_i}, \vec{x_j}\right) \\ s.t. \sum\limits_{i=1}^{m} a_i y_i = 0 \\ C \geq a_i \geq 0, i = 1, 2, \cdots m \end{cases} \tag{22}$$

In the equation, $K(\vec{x_i}, \vec{x_j})$ represents the kernel function.

The final classification decision function is obtained:

$$f(\vec{x}) = sgn(\sum_{i=1}^{m} \alpha_i y_i K(\vec{x_i}, \vec{x}) + b) \tag{23}$$

The Least Squares Support Vector Machine (LS-SVM) replaces the inequality constraints with equality constraints and transforms the quadratic programming problem into solving a set of linear equations. For individual outliers, the variable ξ is introduced, and γ

is the penalty factor defined as the regularization parameter. The expression of LS-SVM is as follows:

$$\begin{cases} \min(\vec{\omega}, \xi) = \frac{1}{2}\left\|\vec{\omega}\right\|^2 + \frac{\gamma}{2}\sum_{i=1}^{l} \xi_i^2 \\ s.t. y_i = \vec{\omega}^T \cdot \phi(\vec{x_i}) + b + \xi_i, i = 1, 2, \cdots i \end{cases} \tag{24}$$

where $\phi(\vec{x})$ is the mapping of the sample eigenvector to a high latitude. The Lagrange function is introduced to obtain:

$$L(\vec{\omega}, b, \xi_i, \alpha_i) = \frac{1}{2}\vec{\omega}^T\vec{\omega} + \frac{\gamma}{2}\sum_{i=1}^{N}\xi_i^2 - \sum_{i=1}^{N}\alpha_i(\vec{\omega}^T\phi(\vec{x_i}) + b + \xi_i - y_i) \tag{25}$$

In Equation (25), α_i is the Lagrange multiplier. Taking the partial derivative of $\vec{\omega}, b, \xi_i, \alpha_i$ and eliminating $\vec{\omega}, \xi$, we obtain the matrix:

$$\begin{bmatrix} 0 & \nu^T \\ \nu & K + \gamma^{-1}I \end{bmatrix}\begin{bmatrix} b \\ \alpha \end{bmatrix} = \begin{bmatrix} 0 \\ Y \end{bmatrix} \tag{26}$$

In Equation (26), $\nu = \begin{bmatrix} 1 & 1 & \cdots & 1 \end{bmatrix}^T$, I is the identity matrix, $\vec{\alpha} = \begin{bmatrix} \alpha_1 & \alpha_2 & \cdots & \alpha_N \end{bmatrix}^T$, $Y = \begin{bmatrix} y_1 & y_2 & \cdots & y_N \end{bmatrix}^T$.

Where K is an N-dimensional square matrix. $K_{il} = \phi(\vec{x_i})^T\phi(\vec{x_j}) = K(\vec{x_i}, \vec{x_j})$, and the predictive function for the LS-SVM model is as follows:

$$f(\vec{x}) = \sum_{i=1}^{N} a_i K(\vec{x_i}, \vec{x_j}) + b \tag{27}$$

Among them, $K(\vec{x_i}, \vec{x_j})$ represents the Gaussian radial kernel function, and its expression is as follows:

$$K(\vec{x_i}, \vec{x_j}) = \exp\left[-\left\|\vec{x_i} - \vec{x_j}\right\|^2 / 2\sigma^2\right]$$

where σ is the bandwidth of the Gaussian radial kernel function.

Sample set D was established, which included the influencing factors as signal frequency f, tunnel section shape and size a, path length d from the transmitting end, and vector representation as $\vec{x} = (f, a, d, \cdots)$. The output y is the correction factor ΔL.

3. Simulation Testing

Since the space in an underground coal mine is limited, the intrinsic safety of underground coal mines has significant impacts on the wireless transmission power and antenna gain; the working frequency of mine wireless signals should be 700 MHz. Compared with other working frequencies, the wireless signal at 700 MHz has the advantages of low wireless transmission energy loss and long distance, can reduce the number of base stations, and has the advantage of low networking costs [29].

The rectangular roadway model can be described using 3D Cartesian coordinates, where x is the horizontal direction of the roadway, y is the direction along the tunnel, and z is the vertical direction. The roadway is 5 m in width, 4 m in height, 20° in tilt angle, and 2000 m in length. The wavelength of a wireless signal with a frequency of 700 Hz is 0.43 m. In the horizontal and vertical direction of the roadway do not meet the condition that the geometric dimensions of the object must be larger than the wavelength, but the longitudinal size of the roadway reaches 2000 m, thus the 700 MHz wireless signal in this direction satisfies the conditions. The signal transmitting end (Tx) and receiving end (Rx) are located at half the width and half the height of the roadway, respectively. A roadway cross section with a height of one half is selected to measure the field strength distribution of wireless signals in the roadway.

1. Signal frequency

The signal frequency has a significant impact on the transmission characteristics of wireless signals in roadways. Figures 4–6 show the attenuation of the wireless signal at 1 GHz, 700 MHz, and 500 MHz, respectively. The signal power distribution curve can be divided into a near-source region and a far-source region. As shown in Figure 4, the signal attenuates rapidly and fluctuates largely in the near-source region, while the signal fluctuation amplitude gradually decreases in the far-source region and gradually stabilizes. This is because there are different modes in the signal. The high-order modes and low-order modes comprehensively affect the strength of the wireless signal at the receiving point. The high-order modes attenuate rapidly in the near source region, resulting in a rapid decrease in signal strength and large signal fluctuations. In the near source region, the low-order modes are less affected by the environment, and the waveform is stable. The signal frequency is the main factor affecting the waveform distribution. The higher the signal frequency is, the farther the boundary point between the near-source region and the far-source region from the signal transmitting end, and the slower the signal attenuation. As shown in Figure 4, the greater the frequency of the wireless signal in the roadway is, the larger the near the source region, and the slower the signal attenuation.

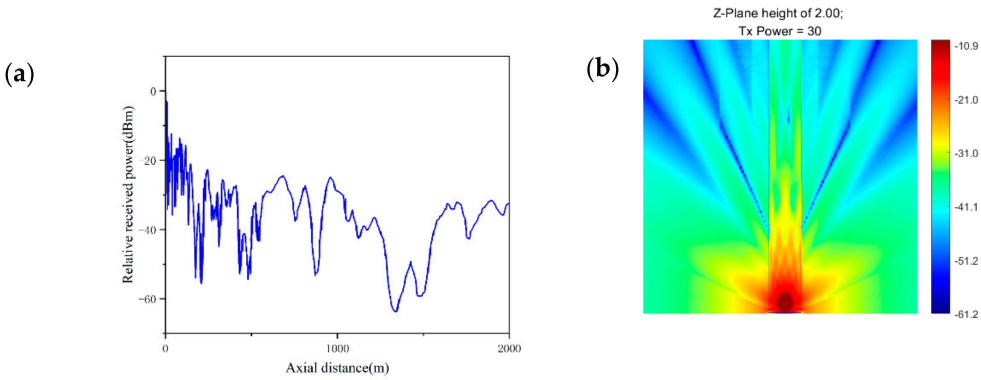

Figure 4. Rx received power when Tx is 1 GHz; (**a**) 1 GH field strength line chart; (**b**) 1 GH field strength distribution map.

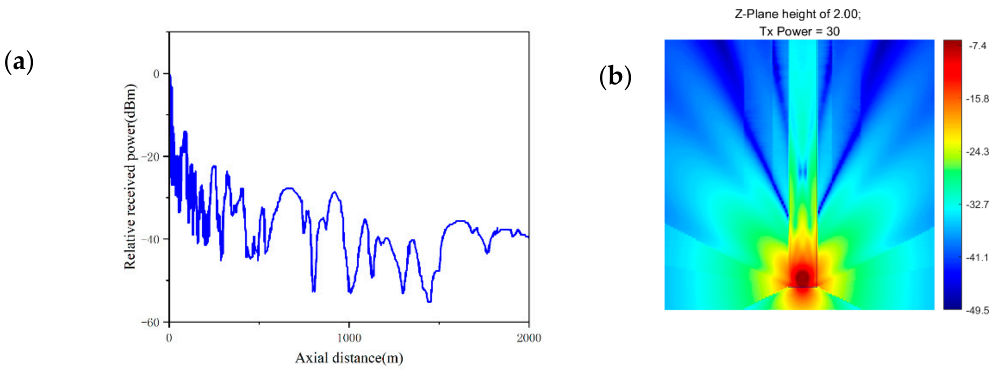

Figure 5. Rx received power when Tx is 700 Hz; (**a**) 700 Hz field strength line chart; (**b**) 700 Hz field strength distribution map.

2. Comparison of the two signal reflections

As shown in Figure 7, the effect of the number of reflections on the transmission of a wireless signal at a frequency of 700 MHz is measured. The reflection coefficient depends on factors such as roadway wall roughness and roadway wall electrical parameters. The reflection coefficient of the signal in the roadway is lower than the reflection coefficient of the normal environment. The comprehensive reflection coefficient is the product of the number of reflections, so the signal strength after multiple reflections makes a relatively small contribution to the field strength at the receiving point (Rx). Figure 7a,b show that the signal strength contributed by the secondary reflected signal in the roadway is far less than the contribution of the primary reflected signal. Therefore, the roughness of the roadway has a significant impact on the number of reflections selected; the greater the number of wireless signal reflections, the smaller is the contribution to the total field strength in the roadway.

(**a**) (**b**)

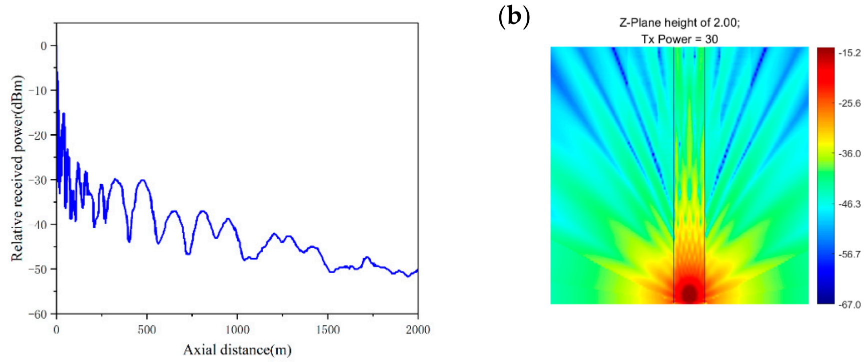

Figure 6. Rx received power when Tx is 500 Hz; (**a**) 500 Hz field strength line chart; (**b**) 500 Hz field strength distribution map.

(**a**)

(**b**)

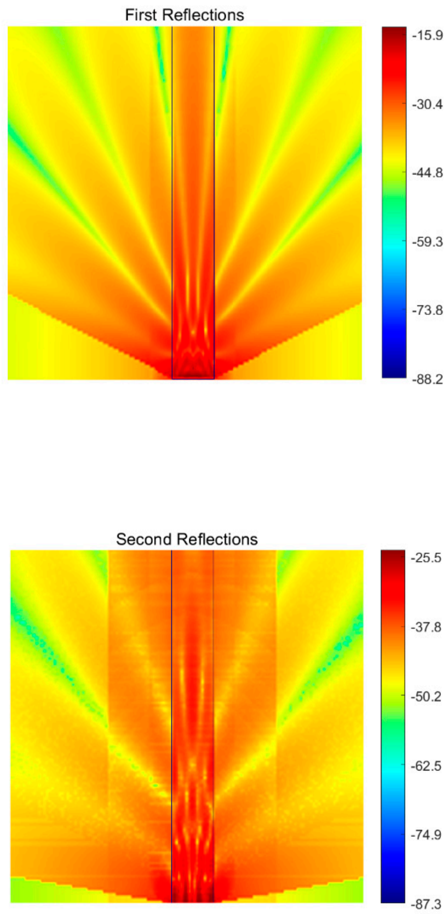

Figure 7. Signal strength at different number of reflections; (**a**) the first reflection of the roadway. signal strength; (**b**) the second reflection of the roadway signal strength.

3. Antenna location

When the transmitting antenna is set close to the roadway wall at one eighth of the width and half of the height, and the transmitting end is located on the same plane, the strength of the wireless signal in the roadway is shown in Figure 8.

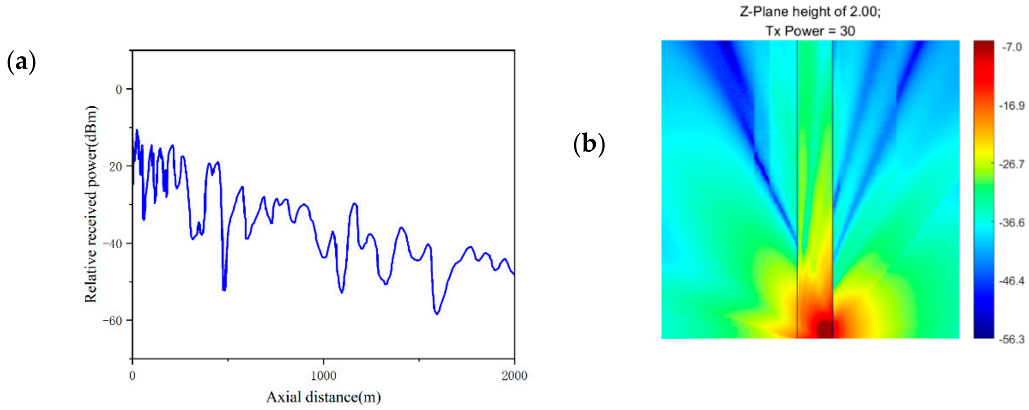

Figure 8. Rx receives power when Tx is close to the roadway wall; (**a**) line diagram of field strength near the roadway wall; (**b**) near the roadway wall field strong cloud map.

A comparison of Figures 5 and 8 reveals that when the transmitting end and receiving end are located in the center of the roadway, the attenuation of the wireless signal is relatively low, and the fluctuation is relatively stable; when the transmitting end is close to the roadway wall, the signal attenuates more dramatically and fluctuates more significantly.

4. Experimental Results

To verify the accuracy of the established roadway model in reflecting the transmission characteristics of wireless signals, an experimental study was conducted. The Ganhe Huozhou Coal Mine has been in operation for 10 years and is a coal mine with low amounts of gas. In this test, the roadway is dark and humid, the inner wall is very rough, and the roadway is covered by cables, pipelines, ventilation and drainage pipes, and supporting metal mesh. Coal seams can be seen through the supporting mesh, and the roadway has a turning point of non-line-of-sight propagation; thus, a good waveguide cannot be formed. The roadway is approximately 1.1 km deep, and the maximum drop can reach 40 m. The locations of the transmitting and receiving ends in the roadway are shown in Figure 9. Table 1 lists the detected signal strengths.

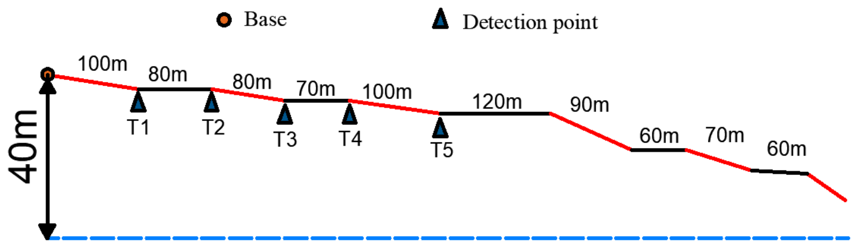

Figure 9. Diagram of the distribution of transceivers in the roadway.

Table 1. Wireless signal strength test results [1].

700 HMz	Downlink Received Power	Downlink Data Throughput	Uplink Received Power	Upstream Data Throughput
T1	−49.1 dBm	14.6 Mbps	−50.9 dBm	14.0 bps
T2	−69.5 dBm	8.1 Mbps	−70.7 dBm	8.1 bps
T3	−86.0 dBm	4.7 Mbps	−88.0 dBm	4.8 bps
T4	N/A	N/A	N/A	N/A
T5	N/A	N/A	N/A	N/A

[1]—The signal could not be connected at T4 and T5. N/A means that the test project does not need to be completed.

The simulation and measurement results of the wireless signal strength are shown in Figure 10. In the visible direction of the slope or flat line, the signal attenuation is gentle, while at the non-line-of-sight roadway turning point, a large amount of signal is absorbed, resulting in substantial attenuation. For a certain distance before the turning point, the wireless signal strength increases because a large number of wireless signal paths could not propagate downward at the turning point, resulting in an aggregation phenomenon, which enhances the signal strength. By fitting the simulation curve, the trend of the wireless signal is found to be basically consistent with the trend of the measured signal strength. The results show that the model created by the 3D ray-tracing method can predict the field strength distribution of wireless signals.

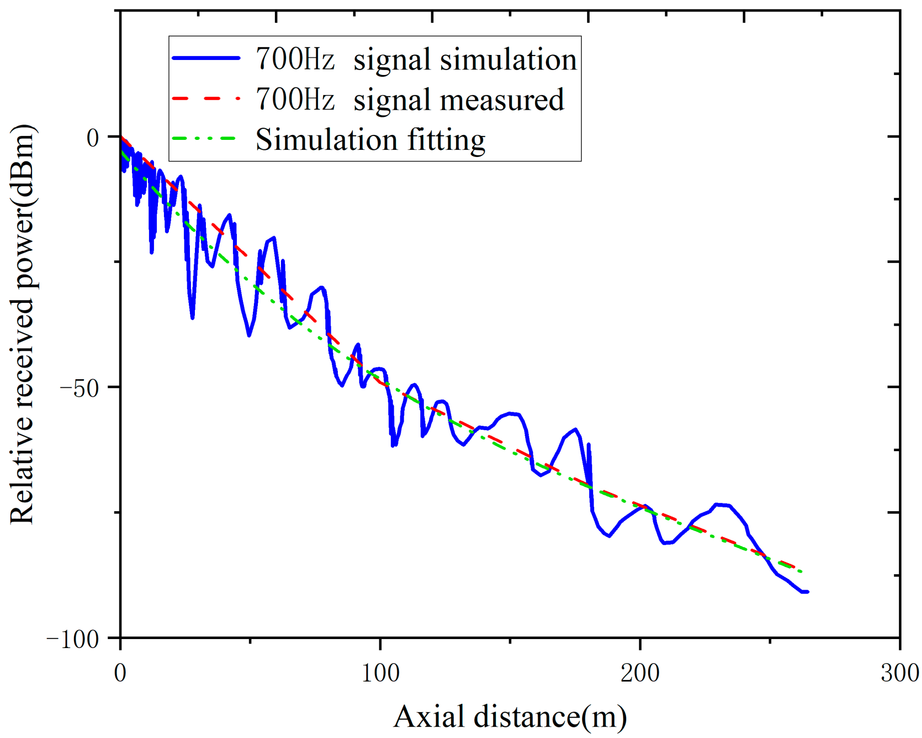

Figure 10. Signal strength simulation and actual measurement.

5. Conclusions

In this paper, the 3D ray-tracing method is used to simulate and analyze the transmission of wireless signals in a roadway:

1. The spatial segmentation-based acceleration algorithm is used to segment the roadway model, which reduces the number of collisions during the path search process and improves the computational efficiency of the 3D ray-tracing method.
2. The results show that, for a wireless signal with a frequency of 700 MHz, the model can accurately reflect the waveform change and attenuation of the wireless signal during signal transmission in the roadway. However, the simulation model only considers relatively basic rectangular, long, straight roadways. In actual production operations, the cross-sectional shapes are trapezoidal and arched, and the roadway has L-shaped right angles and curvatures. This 3D ray tracing only includes the direct and reflected rays, and scattering and diffraction are not taken into consideration. Improvement of the roadway model and the propagation method of wireless signals in the 3D tracking method needs to be carried out in the future.

Author Contributions: Conceptualization, M.Z. and T.D.; methodology, Y.S.; software, B.L.; validation, B.L., T.D. and Y.S.; formal analysis, Y.S.; investigation, Z.N. and Q.W.; resources, Y.S. and T.D.; data curation, B.L.; writing—original draft preparation, B.L.; writing—review and editing, B.L., T.D. and Y.S.; visualization, Y.W.; supervision, Y.W.; project administration, T.D. and Y.S.;

funding acquisition, M.Z. and Z.N. All authors have read and agreed to the published version of the manuscript.

Funding: This research was funded by National Key Research and Development Program of China (2022YFC2904005), National Natural Science Foundation of China (U20A20148), Science and Technology Major Project of the Tibet Autonomous Region's Science and Technology Plan (XZ202201ZD0004G01).

Institutional Review Board Statement: Not applicable.

Informed Consent Statement: Not applicable.

Data Availability Statement: The data presented in this study are available in article.

Acknowledgments: Authors would like to express their gratitude to Zheng Mianping, for his review of the article and valuable feedback. The authors wish him a happy 90th birthday.

Conflicts of Interest: The authors declare no conflicts of interest.

References

1. Arnold, B. A review of element partitioning in coal preparation. *Int. J. Coal Geol.* **2023**, *274*, 104296. [CrossRef]
2. Wang, C.; Cheng, Y. Role of coal deformation energy in coal and gas outburst: A review. *Fuel* **2023**, *332*, 126019. [CrossRef]
3. Raul, R.N.; Palit, S.; Maity, T. Challenges and Viability of Use of PLC for Personal Communication in Underground Coal Mines. *IETE Tech. Rev.* **2021**, *38*, 418–428. [CrossRef]
4. Wu, X.; Li, H.; Wang, B.; Zhu, M. Review on Improvements to the Safety Level of Coal Mines by Applying Intelligent Coal Mining. *Sustainability* **2022**, *14*, 16400. [CrossRef]
5. Wu, B.; Wang, J.; Zhong, M.; Xu, C.; Qu, B. Multidimensional Analysis of Coal Mine Safety Accidents in China—70 Years Review. *Min. Metall. Explor.* **2023**, *40*, 253–262. [CrossRef]
6. Fan, Q.; Yan, X.; Zhang, Y. Design and Realization of the Safety Production Scheduling System. *Res. J. Appl. Sci. Eng. Technol.* **2013**, *5*, 639–645. [CrossRef]
7. Zhang, Y.; Yang, W.; Han, D.; Kim, Y.-I. An integrated environment monitoring system for underground coal mines—Wireless sensor network subsystem with multi-parameter monitoring. *Sensors* **2014**, *14*, 13149–13170. [CrossRef] [PubMed]
8. Dohare, Y.S.; Maity, T.; Das, P.S.; Paul, P.S. Wireless communication and environment monitoring in underground coal mines—Review. *IETE Tech. Rev.* **2015**, *32*, 140–150. [CrossRef]
9. Singh, A.; Kumar, D.; Hötzel, J. IoT Based information and communication system for enhancing underground mines safety and productivity: Genesis, taxonomy and open issues. *Ad Hoc Netw.* **2018**, *78*, 115–129. [CrossRef]
10. Kilinc, F.S.; Monaghan, W.D.; Powell, J.B. A review of mine rescue ensembles for underground coal mining in the United States. *J. Eng. Fibers Fabr.* **2014**, *9*, 155892501400900120. [CrossRef]
11. Khanzode, V.V.; Maiti, J.; Ray, P.K. A methodology for evaluation and monitoring of recurring hazards in underground coal mining. *Saf. Sci.* **2011**, *49*, 1172–1179. [CrossRef]
12. Li, M.; Liu, Y. Underground coal mine monitoring with wireless sensor networks. *ACM Trans. Sens. Netw.* **2009**, *5*, 10. [CrossRef]
13. Ranjan, A.; Sahu, H.B.; Misra, P. Modeling and measurements for wireless communication networks in underground mine environments. *Measurement* **2020**, *149*, 106980. [CrossRef]
14. Zhao, H.; Yang, W. An emergency rescue communication system and environmental monitoring subsystem for underground coal mine based on wireless mesh network. *Int. J. Distrib. Sens. Netw.* **2018**, *14*, 1550147718805935. [CrossRef]
15. Moridi, M.A.; Kawamura, Y.; Sharifzadeh, M.; Chanda, E.K.; Wagner, M.; Jang, H.; Okawa, H. Development of underground mine monitoring and communication system integrated ZigBee and GIS. *Int. J. Min. Sci. Technol.* **2015**, *25*, 811–818. [CrossRef]
16. Zhao, Y.P.; Zhang, J.; Li, J.X.; Tan, Z.H. Simulation of wireless channel in tunnel environment based on improved ray tracing method. *J. Beijing Jiaotong Univ.* **2014**, *38*, 12–18. (In Chinese)
17. Mi, G.S.; Yang, W. Prediction of electromagnetic wave propagation field strength in semi-circular arch mine roadway based on mirror image principle. *J. China Coal Soc.* **2020**, *45* (Suppl. S2), 1089–1099. (In Chinese) [CrossRef]
18. Yao, S.H. Multipath channel model of electromagnetic wave in mine tunnel based on mirror method. *J. Mine Autom.* **2017**, *43*, 46–49. (In Chinese) [CrossRef]
19. Chen, S.-H.; Jeng, S.-K. SBR image approach for radio wave propagation in tunnels with and without traffic. *IEEE Trans. Veh. Technol.* **1996**, *45*, 570–578. [CrossRef]
20. Wang, A.; Ren, C. Prediction of receiving field strength based on SVM-LSTM hybrid model in the coal mine. In Proceedings of the 2021 International Conference on Communications, Information System and Computer Engineering (CISCE), Beijing, China, 14–16 May 2021; pp. 813–816.
21. Wang, A.; Lei, S. Research on modeling of underground path loss prediction based on SA-SVM. *J. Phys. Conf. Ser.* **2022**, *2245*, 012016. [CrossRef]
22. Sun, Z.; Akyildiz, I.F. Channel modeling and analysis for wireless networks in underground mines and road tunnels. *IEEE Trans. Commun.* **2010**, *58*, 1758–1768. [CrossRef]

23. Kasdorf, S.; Troksa, B.; Key, C.; Harmon, J.; Notaros, B.M. Advancing accuracy of shooting and bouncing rays method for ray-tracing propagation modeling based on novel approaches to ray cone angle calculation. *IEEE Trans. Antennas Propag.* **2021**, *69*, 4808–4815. [CrossRef]
24. Wu, M.; Ma, Y.; Zhu, Z. Ray Tracing-Based Wireless Channel Modeling in Room-and-Pillar Mines. In Proceedings of the 2021 IEEE Wireless Communications and Networking Conference (WCNC), Nanjing, China, 29 March–1 April 2021; pp. 1–6.
25. Zheng, X.; Wang, H.; Wen, H.; Guo, J. Propagation characteristics of electromagnetic waves in mine roadways. *J. Appl. Geophys.* **2020**, *173*, 103922. [CrossRef]
26. Mahmoud, S.F.; Wait, J.R. Geometrical optical approach for electromagnetic wave propagation in rectangular mine tunnels. *Radio Sci.* **1974**, *9*, 1147–1158. [CrossRef]
27. Chauhan, V.K.; Dahiya, K.; Sharma, A. Problem formulations and solvers in linear SVM: A review. *Artif. Intell. Rev.* **2019**, *52*, 803–855. [CrossRef]
28. Chen, P.; Xie, Y.; Jin, P.; Zhang, D. A wireless sensor data-based coal mine gas monitoring algorithm with least squares support vector machines optimized by swarm intelligence techniques. *Int. J. Distrib. Sens. Netw.* **2018**, *14*, 1550147718777440. [CrossRef]
29. Sun, J.P.; Zhang, G.M. Research on 5G frequency band selection and antenna optimization setting for mine. *J. Mine Autom.* **2020**, *46*, 1–7. (In Chinese) [CrossRef]